A New Low-Frequency Oscillation Suppression Method Based on EMU On-Board Energy Storage Device

TENG LI, (Member, IEEE), **YONGJUN ZHOU**, **MINGLI WU**, (Member, IEEE), **AND TINGTING HE**

School of Electrical Engineering, Beijing Jiaotong University, Beijing 100044, China

Corresponding authors: Teng Li (liteng@bjtu.edu.cn) and Tingting He (hetingting@bjtu.edu.cn)

ABSTRACT Low frequency oscillation (LFO) in the electric multiple units (EMUs)-traction network cascade system (ETNCS) can lead to traction blockade and abnormal operation. Using the Chinese CRH3 EMUs as an example, a new LFO suppressing method by applying the energy storage (ES) device on EMUs is proposed in this paper and the ES is connected to the DC-link on board. The equivalent model of the ETNCS is established at first. The critical condition of LFO in the ETNCS is analyzed via impedance ratio criterion and Bode diagram. Then, the proposed on-board bidirectional DC-DC converter integrated with the ES system is controlled via a virtual DC machine (VDCM) strategy, and the VDCM small signal model derivation and the parameter design are carried out. Using the Bode diagram of the impedance ratio, the system stability with the ES device controlled by the proposed VDCM scheme is analyzed again; simulation results verify the effectiveness of the control algorithm to suppress the LFO adaptively. Compared with the traditional PI controller, the system steady-state and dynamic performance can be improved with the proposed method, including decreased overshoot, fluctuation, response time, and increased gain margin of the DC-link voltage.

INDEX TERMS Traction power supply, electric multiple units traction network cascade system, low frequency oscillation, energy storage, super capacitor, virtual DC machine, stability analysis.

I. INTRODUCTION

Due to the electrical parameter mismatch of the electric multiple units (EMUs) and the traction network, network voltage and current fluctuations, and corresponding over-voltage or over-current traction blockade caused by Low frequency oscillation (LFO) occurred frequently in recent years [1]–[6]. Both the voltage and current of the traction network were modulated by low frequency waves depending on the types and locations of EMUs on line. Frequencies of the LFO in some countries were mainly concentrated in the band between 10% to 30% of the network fundamental frequency [7]. However, in China, a lower frequency band was found between 3 to 7 Hz, which was around 6% to 14% of the network fundamental frequency [8].

The associate editor coordinating the review of this manuscript and approving it for publication was Shuaihu Li.

Time-domain analysis [9], pole analysis [4], [6], [10], impedance analysis [11]–[15], have been applied to reveal the mechanism of the LFO in the cascade system. It can be found that the LFO is affected by the network-side and train-side, or the 'source'-side and 'load'-side parameters simultaneously. Network-side parameters relate with the capacity of traction substation and the length of the traction network section, which are the representation of the source internal impedance; while the number of running trains, control strategy, topology and control parameters of the Four-Quadrant Converters (4QCs) or the Line-Side Converter (LSC) of certain train are the contribution terms on the train-side impedance. It is impossible for the LFO to occur if the power source is infinite and the source impedance is zero in the ideal assumption. However, the actual power supply cannot be infinite in reality. LFO appears as increasing the number of EMUs connected to the network at the time of operation preparation, i.e., the light load impedance further decreases

because of the EMU parallel connection. In another word, the source is relatively 'weak' compared to the 'strong' load when the LFO appears. From the view of the LSC control strategy of a train, it lacked damping to suppress the disturbance no matter it was the transient current control in the CRH3 or the d-q decoupling control in the CRH5 [16], [17].

In [16], the stability of the cascade system was analyzed by the generalized Nyquist criterion and Bode diagram. Furthermore, system stability estimation based on the coupling impedance of the cascade system was proposed. However, both the analysis and the estimation only considered the internal current control loop. It is not accurate compared to the closed loop analysis considering the outer voltage loop as well. For the CRH5 EMU, an analytical impedance model of the cascade system in the synchronous d-q frame was proposed, which revealed that the Proportional-Integral (PI) controller of the voltage loop control introduced negative damping to the d-d channel impedance of the LSC in the low frequency range [17]. However, the proposed virtual impedance control would affect the dynamic performance of the LSC in the operation state, or high-power state. Similarly, methods of changing the control parameter or strategy, such as adjusting the PI parameter of LSC controller [18], adopting a multivariable control method [19] for the LSC, might not be adaptive to all states, even though they can improve the stability of the cascade system to suppress the LFO at the low-power stage. In [20], [21], Active Disturbance Rejection Controller (ADRC) has been applied in the LSC, the linear PI controller has been changed to non-linear controller, where the parameters change with the feedback error. ADRC is an adaptive controller, it overcomes the contradiction between the overshoot and rapidity of the traditional PI controller, and improves the ability of the controller to suppress large-scale disturbance. However, it is difficult to perform the parameter setting and system stability analysis for this non-linear controller. Another adaptive control strategy of the LSC has been studied to suppress LFO, i.e., a direct power control based on Model Prediction Control (MPC) [22]. In the d-q decoupled system, active power and reactive power predictive control were introduced in the outer voltage loop of the LSC. This method directly controls the predictions of active and reactive power without the need of inner current loop control. However, the DC voltage overshoot was large in the starting stage, and there were high-order harmonics presented in the united simulation of the ETNCS. At the same time, it also lacked the stability analysis of system by using this non-linear control. LFO can also be suppressed by injecting the current with the same oscillation frequency and opposite phase into the system or compensating the oscillation reactive power through Active Power Filter (APF), Static Synchronous Compensator (STATCOM) or Static Var Generator (SVG) [23]–[25]. However, there is the need of the equipment installation at the network high-voltage side, which is expensive.

In conclusion, to suppress the LFO of the cascade system, it is essentially to increase the system damping. It is easier, however very limited, to increase the system damping through changing the control parameters or strategy of the LSC. Furthermore, there is a tradeoff between the adaptability and the practicality to change the control parameters or strategy. Adaptability reflects in two aspects: the LSC control considers both the low-power start-up and high-power operation states; the LSC control adapts different application scenario, such as different types of trains with different controls. Finally, it can even bring additional voltage fluctuation with other frequencies into the system with the improper control parameter setting. For the method of installing additional reactive power compensation device at the network high-voltage side, it is expensive and might also lead to new instability issue if the device is parallel connected with EMUs due to the shortage of inertia in power electronic devices. Therefore, there is still the need to explore one adaptive method to improve the stability and reliability of the cascade system.

When the LFO occurs, not only does the network voltage and current oscillate, but also the DC side voltage of the LSC fluctuates accordingly, which is due to the tracking performance of the LSC control. Therefore, this paper proposes a LFO suppressing method by suppressing the LSC DC side oscillation based on the on-board energy storage (ES) device. Compared to the method of centralized compensation of system overall reactive power, the distributed on-board ES just needs to suppress the DC-link fluctuation of certain motion unit itself, and its capacity is small. Aiming at the system problem of low damping, the virtual DC machine (VDCM) control strategy for the double directional DC-DC converter is proposed. VDCM control simulates the inertia and damping of DC machine and has good steady-state and dynamic performance, which can keep the DC-link voltage stable and further balance the power transport of the LSC. Furthermore, the on-board ES can also be used to store and then regenerate the braking energy of the train. The on-board supercapacitor ES system has been used in China subway train for regenerating the braking energy [26], however, the application of the on-board ES for the EMU train relatively falls behind due to high power and capacity requirement of the ES. China National key Research & Development plan is carrying out the development of high power and density ES power supply on board for hybrid-drive EMUs to provide short-term power by using the regenerated braking energy through ES [27]. The ES capacity requirement to suppress the LFO is much smaller compared to the one for regenerating the energy. Therefore, the proposed on-board ES method for suppressing the LFO is practical and this function can be combined with the energy regeneration function in the later stage.

The rest of this paper is organized as follows. In Section II, the equivalent mathematical model of ETNCS is established by taking the CRH3 as an example. Based on the Middlebrook impedance ratio criterion, the stability of ETNCS is analyzed, and the critical condition for LFO of EMUs is obtained. The LFO suppression strategy based on on-board energy storage is proposed in Section III. The feasibility of
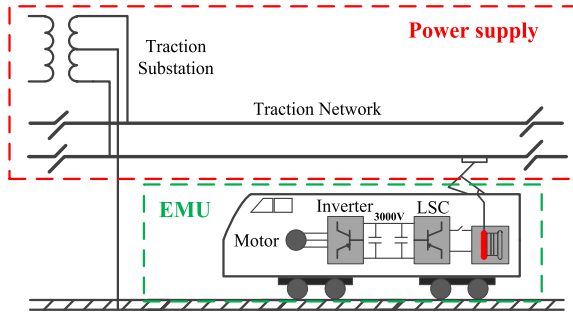
FIGURE 1. Diagram of ETNCS.

the proposed method is verified by the parameter design of the ES device, the modeling and stability analysis of the DC-DC converter control strategy. In Section IV, the ETNCS simulations validate that the proposed control strategy has LFO suppression capability with better steady-state and dynamic performance compared to PI control. Section V draws conclusion for this work.

II. STABILITY MECHANISM ANALYSIS OF (EMUs)-TRACTION NETWORK CASCADE SYSTEM

A. MODELING AND ANALYSIS OF CASCADE SYSTEM CONSIDERING IMPEDANCE MATCHING

Fig. 1 shows the structure diagram of EMU-traction network cascade system (ETNCS), including the traction power supply and one EMU.

The system topology is shown in Fig. 2, where all the parameters are converted to the secondary side of the on-board transformer. The output voltage of the substation transformer U_o is connected with the on-board transformer via the equivalent impedances Z_s and Z_{eq} of the substation transformer and the traction network respectively. The grounding capacitance C_f is connected in parallel with the train input. The power system equivalent impedance Z_{os} in the s-domain can be calculated using (1) [16]. L_n is the equivalent reactance of the on-board transformer. Z_{in} is the equivalent input impedance of the unit 1, which is one of the four power units in CHR3. Thus, the equivalent input impedance of one CRH3 EMU can be expressed as $Z_{in}/4$.

$$Z_{os} = (Z_s + Z_{eq}) \parallel Z_{C_f}$$
$$= (R_l + sL_l) \parallel (s^2 L_l C_f + sR_l C_f + 1) \quad (1)$$

A two-unit topology is shown in Fig. 2 with two H-bridge converter connected in parallel, representing one inverter and four motors. The equivalent resistor R_L is connected on the DC side. R_L is set to 1000 Ω since the LFO occurs at the time with small current and the equivalent load of inverter and motor can be seen as pure resistor. U_{dc} and C_d are the DC-link voltage and supporting capacitor, respectively. L_2 and C_2 are respectively the inductor and capacitor of the second-order filter branch.

A double closed-loop transient current control strategy is used in the CRH3 LSC, as presented in Fig. 3. It is noted that the current reference I_s^* is ignored during the train preparation
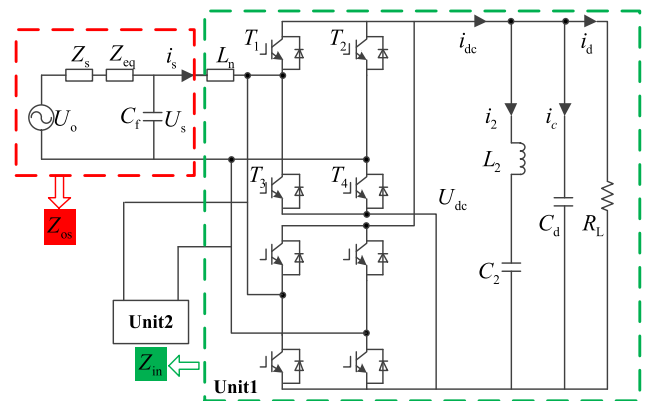

FIGURE 2. Topology of ETNCS.

time due to the small value [28]. U_{dc}^* is the reference voltage of the DC link, U_s and I_s are the network voltage and current respectively. G_1 is the voltage loop PI link; G_2 is the sampling delay link in both the voltage and current loops, and T_v and T_i are the voltage loop and current loop sampling periods respectively; G_3 is the current loop proportional link; G_4 is the PWM modulation transfer function, where T_d is the carrier signal period, where K_{pwm} is the PWM equivalent gain, which is the ratio of modulation wave amplitude to carrier wave amplitude. It is supposed as 1 here; G_5 is the transformer inductor link; G_6 is the switch link, where S_{ab} is the ideal switch gain, which is the average value between the switching function S_a and S_b in a switching cycle. The value of 0.5 is taken in the analysis since the switching function is either in 0 or 1 state; G_7 is the equivalent impedance link of filter, supporting capacitor and load.

Accordingly, the equivalent impedance of the LSC is obtained as follows,

$$Z_{in}(s) = \frac{s^2 L_n(T_v s + 1)(0.5 T_v s + 1)(0.5 T_d s + 1)}{s(0.5 T_v s + 1)\left[(T_v s + 1)(0.5 T_d s + 1) - K_{pwm}\right]}$$
$$+ \frac{K_{pwm} K_{ip}\left[(K_{up} s + K_{ui}) S_{ab} G_7 + s(0.5 T_v s + 1)\right]}{s(0.5 T_v s + 1)\left[(T_v s + 1)(0.5 T_d s + 1) - K_{pwm}\right]} \quad (2)$$

The simplified expression is as follows,

$$Z_{in}(s) = \frac{U_s}{I_s} = \frac{1 + G_3 G_4 G_5 (G_1 G_2 G_6 G_7 + G_2)}{G_5(1 - G_2 G_4)} \quad (3)$$

B. ANALYSIS OF IMPEDANCE RATIO CRITERION

The stability of the ETNCS can be analyzed by using the impedance analysis method for a cascade system [29], [30]. The simplified impedance equivalent model of the ETNCS is shown in Fig. 4.

Then, the traction network voltage is expressed as

$$U_s(s) = U_o(s) \frac{Z_{in}(s)/4}{Z_{in}(s)/4 + Z_{os}(s)} = U_o(s) \frac{1}{1 + T_M(s)} \quad (4)$$

where, $T_M(s) = 4Z_{os}(s)/Z_{in}(s)$ is the ratio of the 'source' output impedance and 'load' input impedance. The system
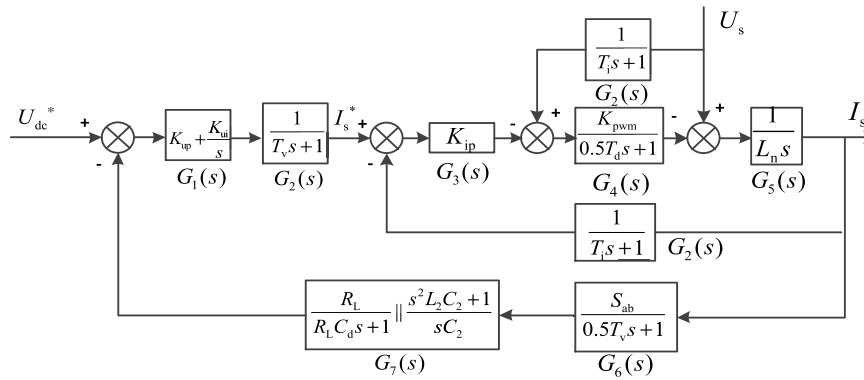
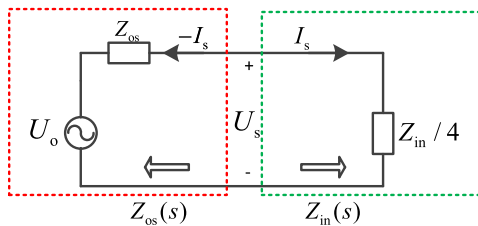**FIGURE 3.** Closed loop control diagram of LSC.

FIGURE 4. Equivalent circuit diagram of source-load.

is stable when $|T_M(s) \ll 1|$ according to the Middlebrook criterion.

With the increase of the number of trains, the equivalent impedance of trains decreases, and $|T_M(s)|$ increases to the value greater than or equal to 1, the ETNCS will become unstable. Suppose n trains are in same position of the traction network for the running preparation, the load impedance for the traction power supply system can be expressed as $Z_{in}/4n$.

Suppose the transformer turns ratio is k, the equivalent impedance Z_{in}' of one EMU converted to the primary side can be described as,

$$Z_{in}' = \frac{k^2 Z_{in}(s)}{4n} \tag{5}$$

Substituting (3) into (5), the impedance ratio of the ETNCS can be written as,

$$T_M = \frac{Z_{os}(s)}{Z_{in}'} = Z_{os}(s)\frac{4nG_5(1 - G_2G_4)}{k^2(1 + G_3G_4G_5(G_1G_2G_6G_7 + G_2))} \tag{6}$$

C. STABILITY ANALYSIS

According to the field test data of LFO in reference [1]–[3], the actual location of LFO, the length of adjacent traction substation, transmission line and the device parameters of LSC are extracted. The parameter of (6) for CRH3 ETNCS is shown in Table 1 for calculating the impedance ratio T_M of the EMU [16].

The Bode diagram of the T_M is shown in Fig. 5 when increasing the number of train from 1 to 6. It can be seen from the Bode magnitude diagram that a peak is shown at the

TABLE 1. Parameters of ETNCS.

Parameters		Description	values
Traction network (TN)	U_o	The secondary voltage of LSC	1550V
	Z_{eq}	Equivalent impedance of TN	6.05+j17.9 mΩ
	Z_s	Equivalent impedance of traction transformer	0.01+j1.96 mΩ
	C_f	Equivalent capacitance of TN	2.81mF
LSC circuit	L_n	Equivalent inductance of on-board transformer	2.3mH
	R_n	Equivalent resistance of on-board transformer	0.1mΩ
	L_2	Secondary filter inductance	0.84mH
	C_2	Secondary filter capacitor	3mF
	C_d	Support capacitor	3.3mF
	U_{dc}	The LSC dc voltage	3000V
	R_L	The load equivalent resistance	1000Ω
PI of LSC	T_v	Voltage sampling time	0.1ms
	T_i	Current sampling time	0.1ms
	T_d	Carrier period	2.85ms
	K_{pwm}	Equivalent gain of PWM	1
	K_{up}	Proportional of voltage controller	0.5
	K_{ui}	Integral of voltage controller	5
	K_{ip}	Proportional of current controller	0.8

low frequency band. With the increase of n, the magnitude Bode plot moves closer to 0 dB, which means the stability of the ETNCS becomes worse. When the number of EMUs is 6, the peak crosses 0 dB line, indicating the instability of the ETNCS and the occurrence of the LFO.

Fig.6 shows the Matlab/Simulink simulation model of the ETNCS, which is used to reproduce the LFO. Network electrical and LSC control parameters are listed in Table 1. The chain network model has been used to simulate network multi-conductor transmission lines, which is an accurate traction network model [16]. In this study, the traction network is equivalent to a resistor and an inductor by Thevenin's theorem to facilitate the analysis as some other LFO analysis models [16], [22].

The Bode diagram analysis shows that the critical condition to occur LFO for the CRH3 is that 6 EMUs raise the pantograph at the same time. Therefore, 5 and 6 EMUs
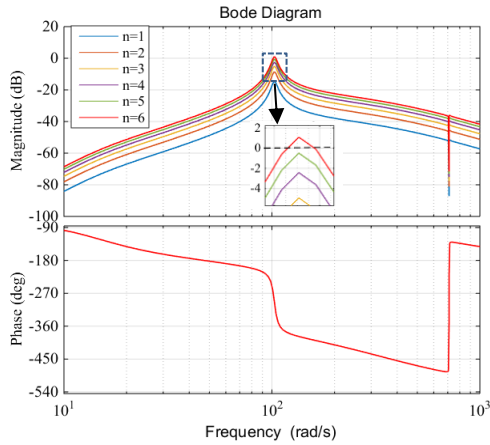
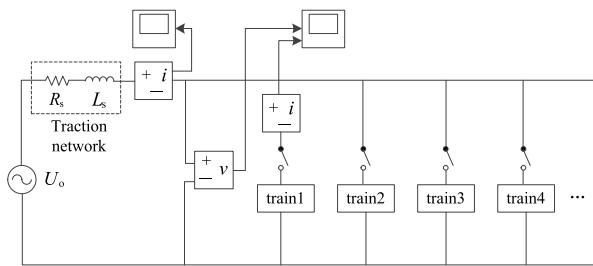**FIGURE 5.** Bode diagram of the impedance ratio of ETNCS.

FIGURE 6. Diagram of train-network cascade system simulation model.

are connected to the traction network respectively in the simulation to show the difference of the voltage and current waveforms at both sides of the train and the network. Fig. 7(a) and (b) show that when 5 EMUs are connected to the traction network at the same time, the electrical quantities at both sides of the train and the network will start to oscillate. After 0.2 s, the oscillations will disappear and the system will return to a stable state. When 6 EMUs are raising the pantograph at the same time, the electrical quantities at both sides of the train and the network will continue to oscillate at a low frequency during all the time. Furthermore, it can be seen that LFO occurs synchronously at all links including the transformer inputs (network voltage and current), the AC inputs and DC outputs of the LSC when 6 EMUs are preparing, which are shown in Fig.7 (c) and (d).

The harmonic spectrum in Fig. 8 (a) shows that the magnitude of harmonic component of the network voltage is very low when the train is running stably. The harmonic spectrum in Fig. 8 (b) shows that the frequencies of the inter harmonics of the network voltage are symmetrically distributed on both sides of the fundamental frequency, which are 44Hz and 56Hz respectively. It indicates that the amplitude of the fundamental wave is modulated by the 6Hz low frequency wave. In addition, there is a 6Hz low-frequency component in the network voltage. The simulation results are consistent with the critical conditions of LFO obtained by theoretical analysis. At the same time, the simulation waveform are close to the measured waveforms in reference [16], which verifies the reliability of the model established in this paper.
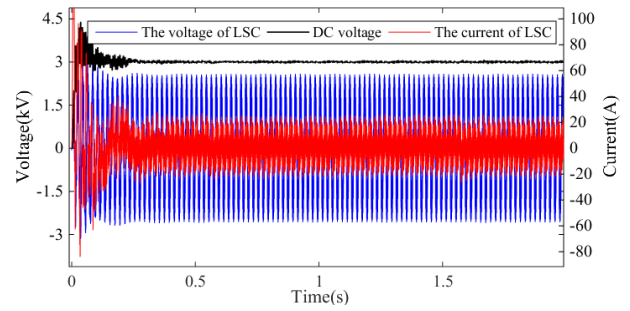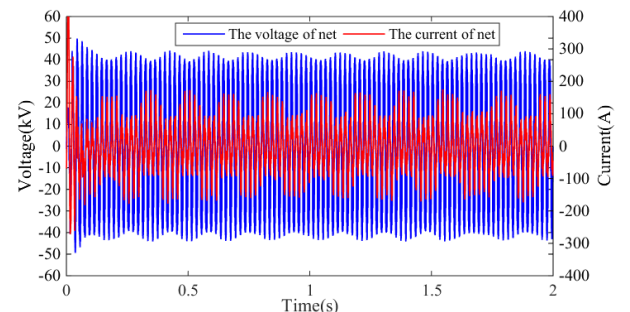

(a) Waveforms of AC inputs and DC voltage output of LSC with 5 EMUs raising pantographs (stable)
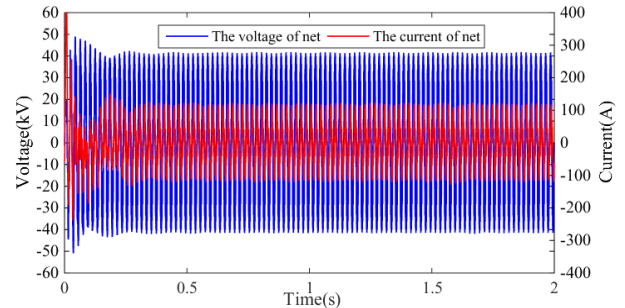
(b) Waveforms of network voltage and current with 5 EMUs raising pantographs (stable)
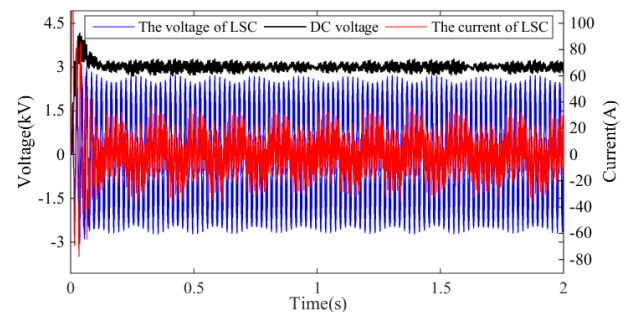
(c) Waveforms of AC inputs and DC voltage output of LSC with 6 EMUs raising pantographs (LFO)


(d) Waveforms of network voltage and current with 6 EMUs raising pantographs (LFO)

FIGURE 7. Waveforms of electrical quantity of the ETNCS.

III. CONTROL STRATEGY OF LOW FREQUENCY OSCILLATION SUPPRESSION BASED ON ON-BOARD ENERGY STORAGE DEVICE

Traditional control methods can be summarized as the impedance match by changing the control parameters or strategy. However, it is difficult to consider both the steady state and dynamic performance of the EMUs. The ES system
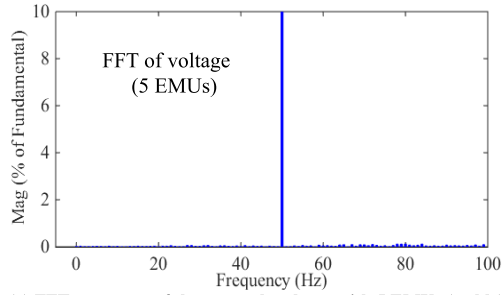
(a) FFT spectrum of the network voltage with 5 EMUs (stable)
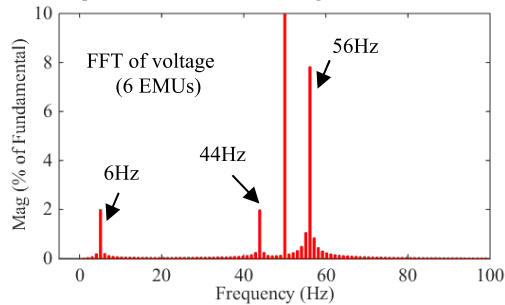
(b) FFT spectrum of the network voltage with 6 EMUs (LFO)

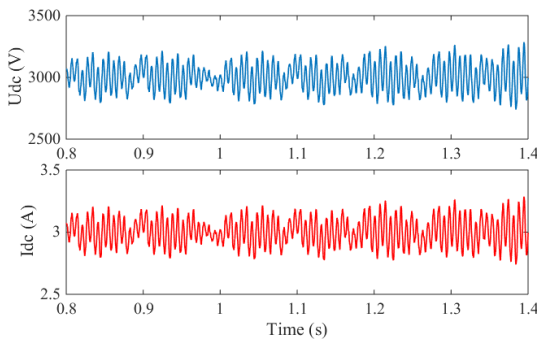**FIGURE 8.** Spectra of the network voltages with the EMU number of 5 and 6.

FIGURE 9. Electrical fluctuation at the DC side of LSC.

FIGURE 10. Power fluctuation of LFO.

FIGURE 11. Structure diagram of ETNCS based on on-board energy storage device.

can compensate the energy exchange during the disturbance stage through certain control strategy, suppressing the power fluctuation and the caused LFO. However, some ES devices such as the battery are not quick enough for compensating a disturbance with quick change [31]. Super-capacitor (SC) has the advantages of long service life, high power density and high charge discharge efficiency. Therefore, SC is chosen as the ES device.

When the LFO occurs, the DC-link voltage and current in the control loop will also show the LFO. The DC voltage and current waveforms and the corresponding power fluctuation in the simulation when the LFO occurs are shown in Fig. 9 and Fig. 10. It can be seen that the DC side power fluctuates in the similar frequency of around 6 Hz as the line side of LSC, and the power peak is 1210 W.

From Fig. 3, it can be seen that the DC voltage is the feedback in the voltage loop of the LSC, so the DC voltage disturbance directly affects the stability of the system. Therefore, it is effective to improve the stability of the DC-link voltage to suppress the LFO. As shown in Fig. 11, the ES device is
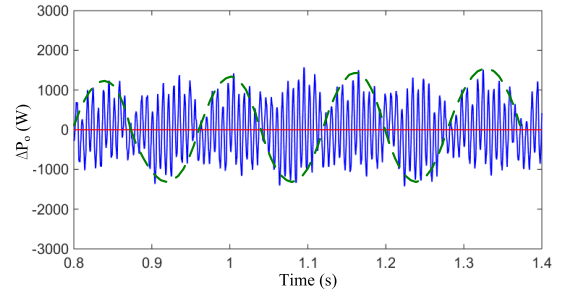
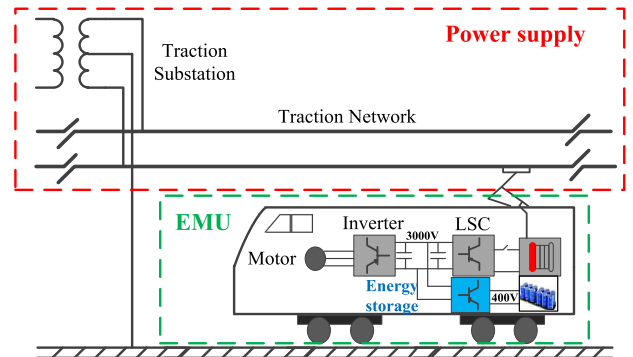now connected with the DC link of the LSC. The ES device will provide a discharging power to compensate the power fluctuation.

The DC-side voltage and power of the LSC respectively are 3000 V and 9000 W during the pantograph lifting preparation. The SC is connected with the DC link through a buck-boost bidirectional DC-DC converter. In order to make the output voltage of the ES converter reach 3000 V quickly, the SC should be charged and discharged continuously. According to the power conservation, the steady value of the discharge current of the SC is 22.5 A; and it should fluctuates around 22.5 A reversely with the DC-link fluctuation.

The capacity of the SC is designed according to the maximum duration of the LFO, which was around 120 s [1], [2]. Therefore, the SC with the total capacity of only 0.75 A·h is needed for each DC link. The total capacitance of 6.75 F can be derived after converting capacity unit of ampere-hour to Coulomb and then dividing by the SC input rated voltage of 400V. Considering the margin, the 8 F SC is chosen for each DC link, corresponding to 150 series connected SCs when a single SC is 1200 F/2.7 V. SC module of BCAP 1200 made by Maxwell Technology Co. Ltd can be selected as the on-board ES device [32]. The parameters are shown in the Table 2. SCs with 150 units have been arranged into a SC pack with the volume of 750*500*108mm. The cost of each ES device is low, containing chassis, SC pack, DC converter, radiator, and control and protect circuits, etc. There are four DC links for each EMU, i.e., four ES devices are needed for each EMU.

Fig. 12 is the topological diagram of the EMU connecting with the ES converter. The VDCM is an effective control

TABLE 2. Parameters of ES device.

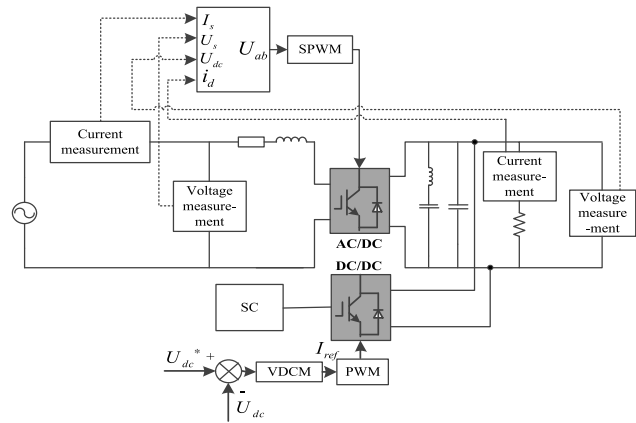| parameters	Values	parameters	Values
rated voltage	2.7V	diameter	50mm
rated capacitance	1200F	height	108mm
maximum capacitance	1440F	number of series	150
ESR_{DC}	0.58mΩ	size of ES	750*500*108mm
usable specific power	5.8kW/kg	weight of ES	39kg

FIGURE 12. Topology of LSC based on on-board energy storage.

method of the bidirectional DC-DC to keep the DC link voltage stable compared to other methods [33]. The traditional double closed-loop control based on PI and droop control [34]–[37] lacks inertia and damping, which makes it limited to keep the stability of the DC-link voltage. Here the VDCM control is used to control the on-board ES converter to verify its function of keeping the DC-link voltage stable through the inertia and damping control; and the ES could provide the suppression energy needed by the control.

A. WORKING PRINCIPLE AND MODEL DERIVATION OF ENERGY STORAGE CONVERTER

In order to avoid frequent charge and discharge of the ES, voltage hysteresis control is applied to determine whether the ES works or not.

As shown in Fig. 13, when DC voltage variation $|\Delta U_{dc}|$ is smaller than 0.1(unit value), it means there is no LFO. Then the state switch $S = 1$, the LSC works normally and there is no need to use the ES. When the DC voltage variation $|\Delta U_{dc}| > 0.1$ (unit value), $S = 2$, the LSC and ES converter work together in the second mode, which means he LFO occurs. The ES converter quickly compensates the fluctuating power to realize the DC voltage stability. The DC voltage signal is then fed back to the voltage loop controller of the LSC; the oscillation signal is compensated to make the control more stable.

The LFO causes the oscillation of the output power ΔP_o of the LSC. In order to suppress the DC power oscillation
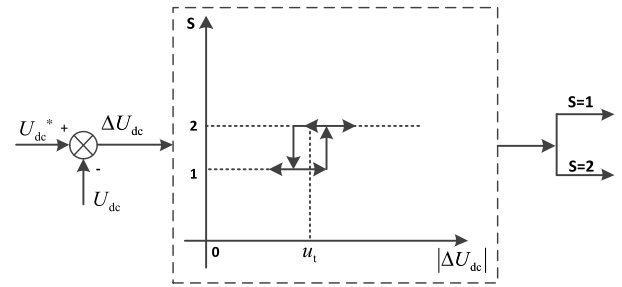

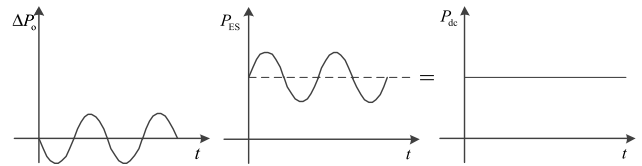**FIGURE 13. Control method of working mode switching.**

FIGURE 14. Schematic diagram of energy storage power compensation.

and then stabilize the DC voltage fluctuation, the ES device should timely output the power P_{ES} opposite to the oscillation power to reach the power balance, which is shown in the Fig. 14.

When the ES controller detects that the actual value of DC-link side voltage is higher than the upper limit threshold $|+\Delta U_{dc}|$ of the given value, the converter works in the buck state; when the ES controller detects that the actual value of DC-link side voltage is lower than the lower limit threshold $|-\Delta U_{dc}|$ of the given value, the converter works in the boost state. The equivalent transformation of its working mode is shown in Fig. 15. Assuming that the flow direction of the inductive current in the buck state of the converter is positive, the inductive current has both positive and reverse directions in one switching cycle. The power flow direction is determined by the integral of the inductive current to the time in one cycle. Therefore, there are four working modes of ES converter in alternate working state.

B. ANALYSIS OF VIRTUAL DC MACHINE

Based on the characteristics of DC machine, the VDCM model of ES converter is shown in Fig. 16. The equivalent two port network of the ES interface converter simulates the inertia and damping characteristics of the DC machine.

E is the armature induced electromotive force; R_a is the equivalent resistance of the armature circuit; I_a is the armature current and it is also the DC-link current; U_{sc} is the SC output voltage; I_{sc} is the SC output current; U_{dc} is the DC-link voltage; C is the capacitor connecting with the DC-link and the value of 3mF is taken for smoothing U_{dc}; P_o is the ES side active power; P_{load} is the exchange power between the ES and DC load.

The VDCM model can be described by the mechanical rotation equation of the DC machine and the potential balance equation of armature circuit, written as,

$$\begin{cases} J\dfrac{d\omega}{dt} = T_m - T_e - D(\omega - \omega_0) \\ T_e = \dfrac{P_e}{\omega} \end{cases} \quad (7)$$
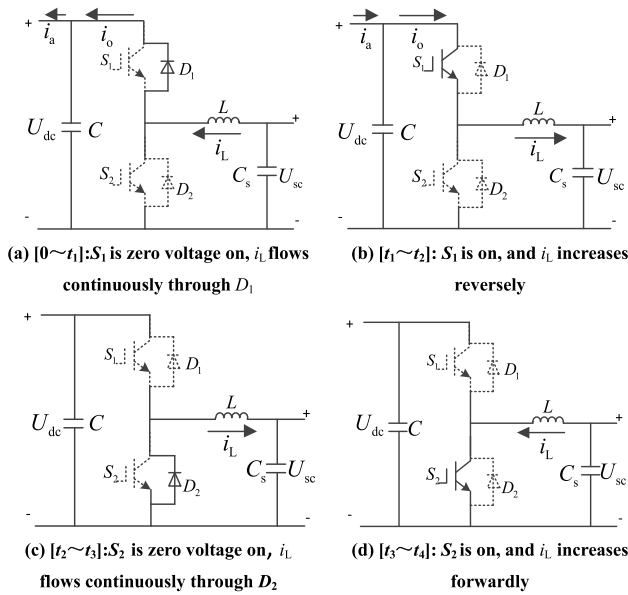
(a) [0~t₁]:S₁ is zero voltage on, i_L flows continuously through D₁

(b) [t₁~t₂]: S₁ is on, and i_L increases reversely

(c) [t₂~t₃]:S₂ is zero voltage on, i_L flows continuously through D₂

(d) [t₃~t₄]: S₂ is on, and i_L increases forwardly

FIGURE 15. Four working states of ES converter in alternating working state.
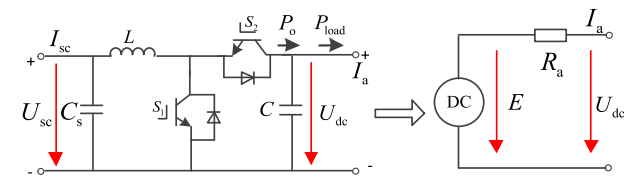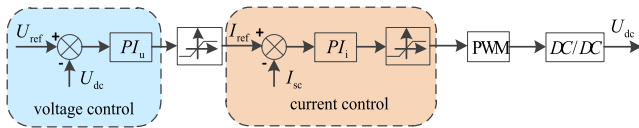

FIGURE 16. Equivalent model of VDCM.

FIGURE 17. Block diagram of traditional double closed loop constant voltage control.

where, J is the moment of inertia, D is the damping coefficient; T_m and T_e is the mechanical torque and electromagnetic torque of the DC machine, respectively, ω is the actual rotational angular speed, ω_0 is the rated angular speed, P_e is the electromagnetic power.

The balance equation of electromotive force is as followed,

$$\begin{cases} U_{dc} = E - R_a I_a \\ E = C_T \Phi \omega \end{cases} \quad (8)$$

where, C_T is the torque coefficient and Φ is the flux per pole.

C. SMALL SIGNAL ANALYSIS AND PARAMETERS

The ES converter adopts traditional double closed-loop constant voltage control, and the block diagram is shown in Fig. 17. The stability of DC voltage can be maintained by adjusting the outer DC voltage loop and the inner current loop, where, U_{ref} is the reference value of DC voltage and I_{ref} is the reference value of inductance current.
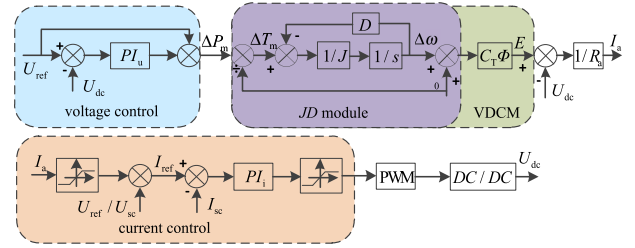

FIGURE 18. Block diagram of VDCM.

On the basis of above traditional control, the VDCM is realized, which is shown in Fig. 18. Where, ΔP is the power deviation; ΔT_m is the torque deviation; $\Delta \omega$ is the angular velocity deviation. In the DC-link voltage regulation part, the link voltage feedback value U_{dc} is compared with the link voltage reference value U_{ref}, and the PI controller of voltage is used to adjust the DC-link voltage and generate the mechanical power deviation ΔP; the VDCM module conducts the control according to the moment of inertia and damping coefficient similar to the characteristics of the DC machine shown in (7) and (8), so as to improve the stability of the DC voltage. To balance the power, the current regulator converts the armature current to the reference value of the input current through U_{ref}/U_{sc}, and obtains the required control signal through current PI controller and PWM modulation.

Fig. 18 shows that when the DC side load has power fluctuation, the ES converter adjusts the actual angular velocity ω according to the mechanical rotation equation, and then adjusts the induced electromotive force E to respond to the corresponding voltage disturbance.

Combine (7) and (8), let $\Delta \omega = \omega - \omega_0$, it follows that,

$$J \Delta \dot{\omega} = T_m - \frac{C_T^2 \Phi^2 \omega_0}{R_a} - \frac{C_T^2 \Phi^2 \Delta \omega}{R_a} - D \Delta \omega \quad (9)$$

Add disturbance to (9), it follows that,

$$J(\Delta \dot{\omega} + \Delta \hat{\omega}) = (T_m + \hat{T}_m) - \frac{C_T^2 \Phi^2 \omega_0}{R_a} \\ - \frac{C_T^2 \Phi^2 (\Delta \omega + \Delta \hat{\omega})}{R_a} - D(\Delta \omega + \Delta \hat{\omega}) \quad (10)$$

Separate the disturbance and make variable substitution, so that,

$$J \Delta \dot{\omega} = T_m - \frac{C_T^2 \Phi^2 \Delta \omega}{R_a} - D \Delta \omega \quad (11)$$

By performing the Laplace transform of (11), the transfer function of the JD module in the VDCM module is obtained,

$$G_{JD}(s) = \frac{R_a}{J R_a s + (C_T \Phi)^2 + D R_a} \quad (12)$$

Eq. (12) shows that JD module is approximately a first-order inertial link with an ES element, where the rotational inertia J is equivalent to the inertial time constant of the
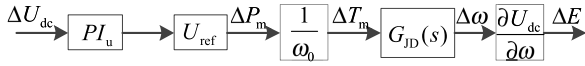
FIGURE 19. Small signal model of VDCM.

first-order inertial link. It can be seen from Fig. 14 that the relationship between DC voltage and power is shown as,

$$CU_{dc}\frac{dU_{dc}}{dt} = P_{load} - P_o \tag{13}$$

Therefore, the voltage fluctuation caused by unbalanced power is mainly related to the DC side capacitance. The larger the capacitance value, the greater the system inertia. However, in the actual DC converter system, the capacitance value is small, which is only 3 mF here; the link voltage is still vulnerable to disturbance.

According to (8), the U_{dc} can be expressed as,

$$U_{dc} = C_T \Phi \omega - I_a R_a \tag{14}$$

Do the angular frequency deviation on both side of (14), the change rate of voltage with angular frequency is obtained,

$$\frac{\partial U_{dc}}{\partial \omega} = C_T \Phi \tag{15}$$

Derived from Fig. 18, the small signal model of the VDCM module is shown in Fig. 19.

The transfer function between the output voltage deviation ΔE of the ES converter and the DC-link voltage deviation ΔU_{dc} is obtained,

$$\begin{aligned} G_{VDCM}(s) &= \frac{\Delta E(s)}{\Delta U_{dc}(s)} \\ &= \frac{U_{ref}C_T \Phi R_a(k_{up\_vdcm}s + k_{ui\_vdcm})}{JR_a\omega_0 s^2 + (C_T^2\Phi^2\omega_0 + DR_a\omega_0)s} \end{aligned} \tag{16}$$

The control parameters should be designed according to the dynamic response of the ES device to suppress the LFO. Fig. 20 shows the root locus chart of the VDCM transfer function. Within a certain value range, the increase of J and D can enhance the stability of the system. In addition, the selection of J and D should make the system poles close to the real axis and away from the virtual axis to avoid large oscillation. However, parameters should also be reasonably designed according to other control requirements. According to the power-frequency droop characteristic of the VDCM, D is the ratio of the electromagnetic torque change and angular frequency change, where the torque corresponds to (7). The expressions can be defined as,

$$D = \frac{\Delta T}{\Delta \omega} = \frac{\Delta P_{set}}{2\pi f_n \cdot 2\pi \Delta f} \tag{17}$$

The power ΔP_{set} at the DC-link is 9000 W, and the torque should fully respond when the oscillation frequency changes in the range of $\pm 2\%$, then D should be 4.6 according to (17).

The value of inertia J is related to the time constant τ_f of the power-frequency regulation. The expressions can be defined as,

$$J = \tau_f \cdot D \tag{18}$$
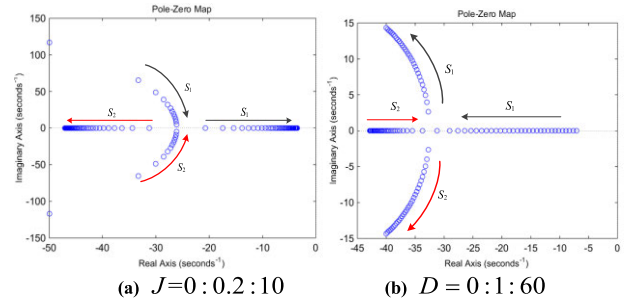

(a) $J = 0:0.2:10$ (b) $D = 0:1:60$

FIGURE 20. Root locus of VDCM with different parameters.

When J is too large, the overshoot may be formed in the response and the response time will be long. Take all above factors into consideration, parameters J and D are designed respectively as 8 and 5.

D. STABILITY ANALYSIS INTEGRATED WITH ENERGY STORAGE

When the ES converter and the LSC work together, according to the proposed control strategy, the ES converter is used to suppress the DC voltage fluctuation, and the DC voltage signal is fed back to the voltage loop of the LSC to suppress the LFO. The control block diagram is shown in Fig. 21.

After further transforming, the transfer function of the equivalent input impedance of the LSC after adding the ES converter can be obtained from Fig. 22, which is shown in (19),

$$Z'_{in}(s) = \frac{U_s}{I_s} = \frac{1 + G_3G_4G_5(G_1G_2G_6G_7G_8 + G_2)}{G_5(1 - G_2G_4)} \tag{19}$$

$$\begin{aligned} T_M &= \frac{Z_{os}(s)}{Z'_{in}} \\ &= Z_{os}(s)\frac{4nG_5(1 - G_2G_4)}{k^2(1 + G_3G_4G_5(G_1G_2G_6G_7G_8 + G_2))} \end{aligned} \tag{20}$$

Therefore, the impedance ratio between the system output impedance and the input impedance of the train is changed to (20) after considering the ES converter. Fig. 23 shows the impedance ratio Bode diagram of the ETNCS under different conditions when 6 trains are lifting the pantographs at the same time. The low-frequency instability point of Bode magnitude diagram decreases from 0 dB to the below of 0 dB. Compared with before compensation, the bandwidth is also increased and the system stability is enhanced.

E. COMPARISON OF VIRTUAL DC MACHINE AND PI CONTROL

Traditional DC-DC control of the ES converter includes the voltage and current double closed-loop PI control and PWM complementary control to realize the bidirectional power regulation [38]. The parameters of the PI and VDCM controller are shown in Table 3. Fig. 24 shows the Bode diagram comparison when the ES converter adopts the VDCM control and the traditional PI control.
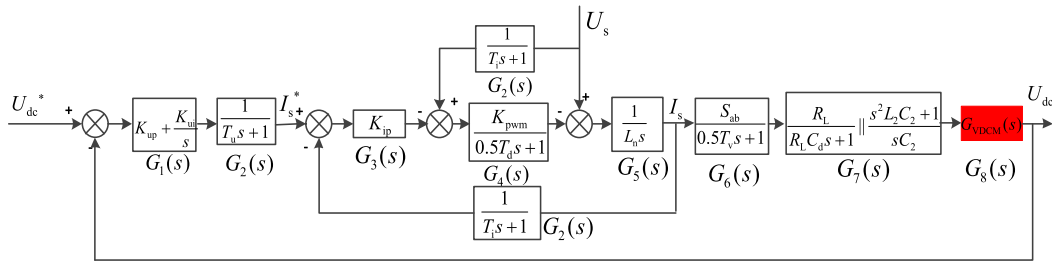
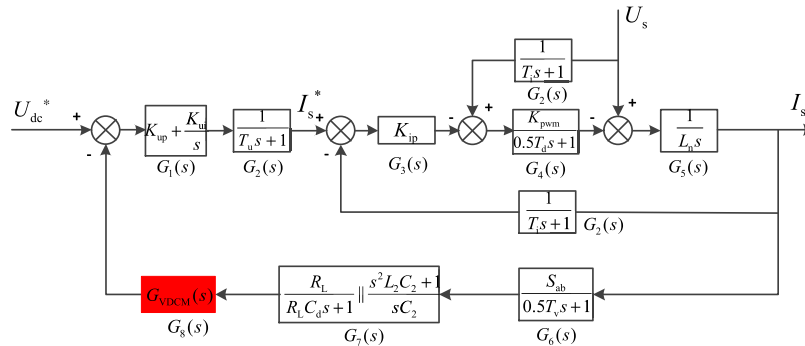**FIGURE 21.** Control block diagram of LSC with coupled on-board energy storage.
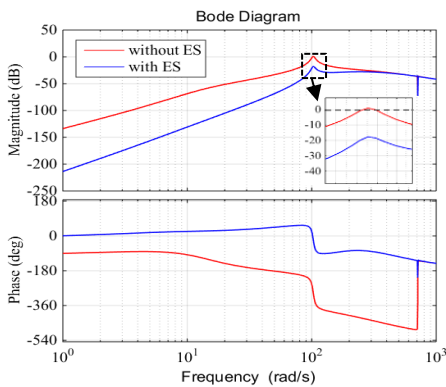

FIGURE 22. Block diagram after transformation.

FIGURE 23. Bode diagram of the impedance ratio of ETNCS after adding on-board energy storage device.

TABLE 3. Parameters of VDCM and PI.

Parameters		Description	values
VDCM control	U_{ref}	DC voltage of LSC	3000V
	U_{SC}	The voltage of SC	400V
	ω_n	Rated angular velocity	100π rad/s
	J	Moment of inertia	8kg·m^2
	D	Damping coefficient	5
	$C_T\Phi$	The product of torque coefficient and flux per pole	9.55
	R_a	Equivalent resistance of armature	0.2Ω
	k_{up_vdcm}	Proportional of VDCM	1
	k_{ui_vdcm}	Integral of VDCM	0.1
	f_s	switching frequency	20 kHz
PI control	k_{up_pi}	Proportional of voltage controller	0.2
	k_{ui_pi}	Integral of voltage controller	15
	K_{ip_pi}	Proportional of current controller	1
	K_{ii_pi}	Integral of current controller	30

TABLE 4. DC voltage control performance comparison of two control strategies.

Method	Overshoot (%)	Settling time/s	Voltage fluctuation/V	gain margin /dB	phase margin /deg
PI	24.3	0.45	±107	22.6	∞
VDCM	7.3	0.15	±29	32.5	∞

Fig.24 shows that when six trains lift the pantographs, the on-board ES based on PI control can make the low-frequency instability point move down to −1.3 dB, which means the system recovers to the stable state after adding the ES device. However, the peak value of the instability point with the VDCM control is reduced to −17.7 dB. What's more, the gain margin of PI control is 22.6 dB, and the gain margin of VDCM is 32.5 dB. The VDCM control strategy can further compensate the damping of the ETNCS by introducing the damping coefficient D, which improves the stability margin of the system.

The DC-link voltage dynamic responses based on these two control methods are compared in Fig. 25. Their performance values are given in Table 4.

It can be seen from Fig. 25 and Table 4 that the voltage overshoot with the ES converter based on the traditional PI
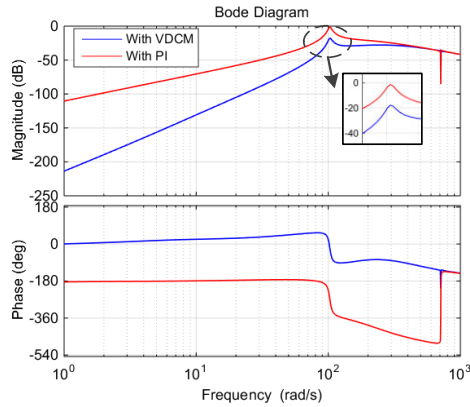
FIGURE 24. Comparison of steady-state stability of two control methods.
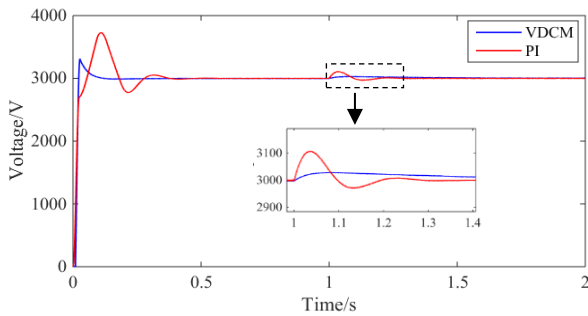

FIGURE 25. DC-link voltage waveforms with two control strategies.

control is 24.3%, and the one based on the VDCM control is only 7.3%; the regulation time based on the VDCM control is 0.15 s, which is faster than the 0.45 s dynamic response speed with the PI control; when there is a disturbance, the voltage fluctuation under PI control is larger, however the VDCM control is less affected. Therefore, the dynamic performance of VDCM control is better than traditional PI control, which can make the system reach the steady state quickly and smoothly.

IV. SIMULATION VERIFICATION

The ETNCS with the on-board ES has been simulated again by using above Matlab/Simulink model shown in Fig.6. Parameters in Table 3 have been used in the PI and VDCM controls of the ES converter.

When 6 or 7 EMUs lifting pantographs at the same time with the light load, the ES device is put into operation at 0.5 s in the simulation. Waveforms of the AC inputs and the DC voltage output of the LSC are shown in Fig. 26.

Fig. 26 shows that the DC-link voltage reaches a stable state within 0.25 s after the ES device is put into operation, and there are no obvious low frequency harmonic components anymore caused by the LFO even when 7 EMUs are raising the pantographs at the same time, which can be seen in Fig.27.

Fig. 28 shows the DC-link voltage waveforms when the ES converter adopts traditional PI and VDCM control strategies. When the ES device is connected to the DC side of LSC at
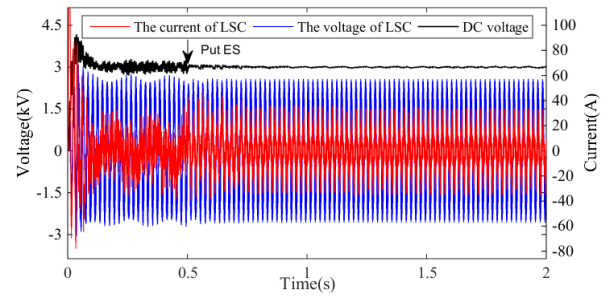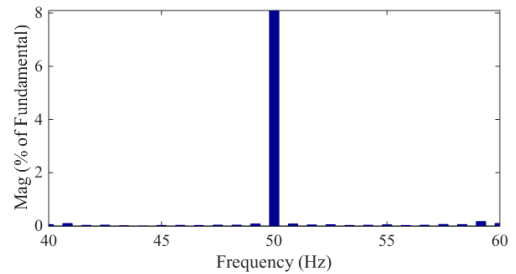

(a) Waveforms of AC inputs and DC voltage output of LSC with 6 EMUs raising pantographs and ES is put in at 0.5 s
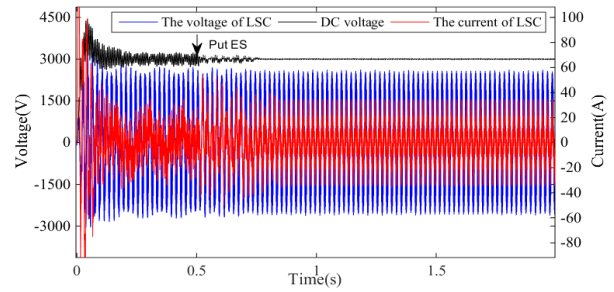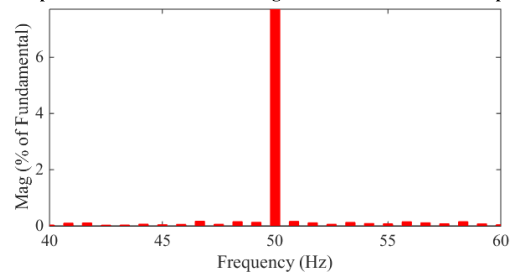

(b) Waveforms of AC inputs and DC voltage output of LSC with 7 EMUs raising pantographs and ES is put in at 0.5 s.

FIGURE 26. Waveforms of electrical quantity of the ETNCS based on on-board energy storage device.

(a) FFT spectrum of the network voltage with 6 EMUs when ES is put in

(b) FFT spectrum of the network voltage with 7 EMUs when ES is put in

FIGURE 27. Spectra of the network voltages of ETNCS based on on-board energy storage device.

0.5 s, the voltage controlled by PI method drops to 2429 V and that controlled by VDCM method is 2767 V. Compared with the traditional PI control, the proposed VDCM control strategy can provide greater damping and appropriate inertia for the system, which makes the DC side voltage dynamic response better and the stability stronger when the ES device is connected to the DC link. It is shown that the ES device based on the VDCM control proposed in this paper can better suppress the LFO of ETNCS.
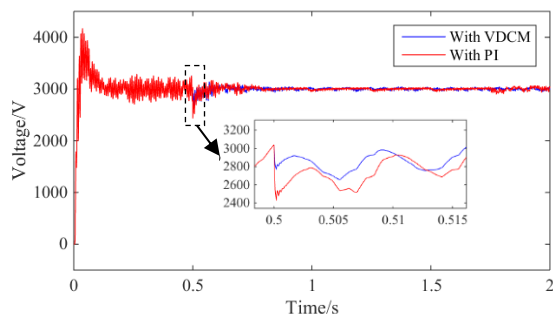
FIGURE 28. DC-link voltage waveforms with different control strategies.
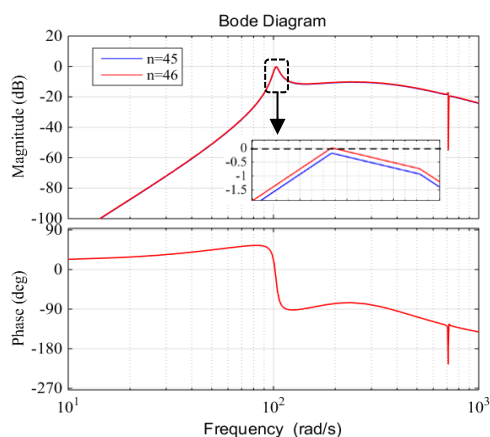

FIGURE 29. LFO critical condition of train number.

Fig. 29 shows the Bode diagram of the ETNCS after adding on-board ES devices. The magnitude curve is below 0 dB and the system is stable when 45 trains raise pantographs at the same time. However, the curve peak passes through 0 dB when 46 trains raise the pantographs simultaneously. Therefore, the critical number of trains without showing the LFO after adding on-board ES devices is 45.

V. CONCLUSION

In order to suppress the LFO, the DC side power compensation strategy of LSC based on on-board energy storage is proposed. Traditional LFO suppression method of changing the LSC control parameters or strategy is neither adaptive nor practical. The ES device discharges according to the DC voltage deviation. The suppressed DC voltage signal is fed back to voltage loop of the LSC to realize feedback damping compensation. Aiming at the problem that the traditional PI control of the ES converter is not sensitive to power disturbance, a VDCM control strategy is proposed to adaptively respond to DC side power fluctuation and maintain DC voltage stability. The stability criteria and simulation results show that the proposed suppression method makes the ETNCS have greater gain margin, which can accommodate more EMUs. In addition, compared with the traditional PI control, the proposed VDCM control strategy has the advantages of small overshoot, short adjustment time and good dynamic performance.

It should be noted that the proposed control strategy is not limited to a single type EMUs, and it can be extended to other systems by a simple redesign of the ES parameters. Further work in this field can consider the optimization of the energy management strategy of the ES after combining the function of braking energy regeneration. On one hand, it can suppress LFO and improve power quality during the start-up stage; on the other hand, it can be responsible for the regeneration of the braking energy during train deceleration operation. The hybrid ES could also be considered in the future for taking account both the high power and high energy density at the same time.

REFERENCES

[1] *Test Report on Matching Relationship of HXD1 Train Network of Daqin Line*, China Academy of Railway Sciences, Beijing, China, 2008.

[2] *CRH1067 Catenary Voltage and Current Test Report*, Shanghai Nanxiang switching office, Beijing, China, 2010.

[3] *Test Report of Catenary Voltage Fluctuation*, Xuzhou North Train Depot, Beijing, China, 2011.

[4] H. Wang, W. Mingli, and J. Sun, "Analysis of low-frequency oscillation in electric railways based on small-signal modeling of vehicle-grid system in DQ frame," *IEEE Trans. Power Electron.*, vol. 30, no. 9, pp. 5318–5330, Sep. 2015.

[5] S. Menth and M. Meyer, "Low frequency power oscillations in electric railway systems," *Elektrische Bahnen.*, vol. 104, no. 4, pp. 216–221, 2006.

[6] S. Danielsen, O. B. Fosso, M. Molinas, J. A. Suul, and T. Toftevaag, "Simplified models of a single-phase power electronic inverter for railway power system stability analysis—Development and evaluation," *Electr. Power Syst. Res.*, vol. 80, no. 2, pp. 204–214, Feb. 2010.

[7] S. Danielsen, M. Molinas, T. Toftevaag, and O. B. Fosso, "Constant power load characteristic's influence on the low-frequency interaction between advanced electrical rail vehicle and railway traction power supply with rotary converters," in *Proc. Modern Electr. Traction (MET)*, Sep. 2009, pp. 89–94.

[8] H. Tao, H. Hu, and X. F. Jiang, "Research on low frequency voltage oscillation in traction power supply system and its affecting factors," *Power Syst. Technol.*, vol. 40, no. 6, pp. 1830–1838, Jun. 2016.

[9] C. Heising, R. Bartelt, M. Oettmeier, V. Staudt, and A. Steimel, "Enhancement of low-frequency system stability of 60-hz railway power grids," in *Proc. 14th Int. Power Electron. Motion Control Conf. EPE-PEMC*, Sep. 2010, pp. S7-1–S7-8.

[10] H. Hu, H. Tao, X. Wang, F. Blaabjerg, Z. He, and S. Gao, "Train–network interactions and stability evaluation in high-speed railways—Part II: Influential factors and verifications," *IEEE Trans. Power Electron.*, vol. 33, no. 6, pp. 4643–4659, Jun. 2018.

[11] J. Suarez, P. Ladoux, N. Roux, H. Caron, and E. Guillame, "Measurement of locomotive input admittance to analyse low frequency instability on AC rail networks," in *Proc. Int. Symp. Power Electron., Electr. Drives, Autom. Motion*, Jun. 2014, pp. 790–795.

[12] S. Pika and S. Danielsen, "Understanding of the stability criterion for a double-feedback loop system," in *Proc. Electr. Syst. Aircr., Railway Ship Propuls.*, Oct. 2010, pp. 1–5.

[13] Y. Liao, Z. Liu, G. Zhang, and C. Xiang, "Vehicle-grid system modeling and stability analysis with forbidden region-based criterion," *IEEE Trans. Power Electron.*, vol. 32, no. 5, pp. 3499–3512, May 2017.

[14] Y. Liao, Z. Liu, H. Zhang, and B. Wen, "Low-frequency stability analysis of single-phase system with DQ-frame impedance approach—Part I: Impedance modeling and verification," *IEEE Trans. Ind. Appl.*, vol. 54, no. 5, pp. 4999–5011, Sep. 2018.

[15] H. Tao, H. Hu, X. Wang, F. Blaabjerg, and Z. He, "Impedance-based harmonic instability assessment in a multiple electric trains and traction network interaction system," *IEEE Trans. Ind. Appl.*, vol. 54, no. 5, pp. 5083–5096, Sep. 2018.

[16] Z. Liu, G. Zhang, and Y. Liao, "Stability research of high-speed railway EMUs and traction network cascade system considering impedance matching," *IEEE Trans. Ind. Appl.*, vol. 52, no. 5, pp. 4315–4326, Sep. 2016.

[17] Y. Zhou, H. Hu, X. Yang, J. Yang, Z. He, and S. Gao, "Low frequency oscillation traceability and suppression in railway electrification systems," *IEEE Trans. Ind. Appl.*, vol. 55, no. 6, pp. 7699–7711, Nov. 2019.

[18] M. Brenna, F. Foiadelli, and D. Zaninelli, "New stability analysis for tuning PI controller of power converters in railway application," *IEEE Trans. Ind. Electron.*, vol. 58, no. 2, pp. 533–543, Feb. 2011.

[19] C. Heising, M. Oettmeier, V. Staudt, A. Steimel, and S. Danielsen, "Improvement of low-frequency railway power system stability using an advanced multivariable control concept," in *Proc. 35th Annu. Conf. IEEE Ind. Electron.*, Nov. 2009, pp. 560–565.

[20] J. Xu, H. Cheng, W. Huang, Y. Liu, Z. Chen, and B. An, "A novel approach based on self-adaptive auto disturbance rejection proportional integral controller to suppress low frequency oscillation of high speed railway electric multiple units-traction network coupling system," *Proc. CSEE*, vol. 38, no. 14, pp. 4035–4045, Jul. 2018.

[21] S. Yao, Z. Liu, and G. Zhang, "A novel approach based on ADRC to traction network voltage low frequency oscillation suppression research," *Power Syst. Technol.*, vol. 40, no. 1, pp. 207–213, Jan. 2016.

[22] Z. Liu, C. Xiang, Y. Wang, Y. Liao, and G. Zhang, "A model-based predictive direct power control for traction line-side converter in high-speed railway," *IEEE Trans. Ind. Appl.*, vol. 53, no. 5, pp. 4934–4943, Sep. 2017.

[23] P.-C. Tan, R. E. Morrison, and D. G. Holmes, "Voltage form factor control and reactive power compensation in a 25-kV electrified railway system using a shunt active filter based on voltage detection," *IEEE Trans. Ind. Appl.*, vol. 39, no. 2, pp. 575–581, Mar. 2003.

[24] G. Wang, H. Sun, X. Zhu, and H. Tan, "Theory and simulation of STATCOM supplementary voltage control to damp sub-synchronous resonance," *Autom. Electr. Power Syst.*, vol. 37, no. 11, pp. 33–38, Jun. 2013.

[25] L. Wang, X. Xie, Q. Jiang, and X. Liu, "Centralised solution for sub-synchronous control interaction of doubly fed induction generators using voltage-sourced converter," *IET Gener., Transmiss. Distrib.*, vol. 9, no. 16, pp. 2751–2759, Dec. 2015.

[26] Y. Fu, N. Zhang, and Y. Mao, "Development of high-power and high-density energy storage power supply for hybrid Electric Multiple Units (EMU)," *Mod. Urban Transit*, no. 7, pp. 29–34, Jul. 2020.

[27] Z. Zhong, Z. Yang, X. Fang, F. Lin, and Z. Tian, "Hierarchical optimization of an on-board supercapacitor energy storage system considering train electric braking characteristics and system loss," *IEEE Trans. Veh. Technol.*, vol. 69, no. 3, pp. 2576–2587, Mar. 2020.

[28] M. Cespedes and J. Sun, "Impedance modeling and analysis of grid-connected voltage-source converters," *IEEE Trans. Power Electron.*, vol. 29, no. 3, pp. 1254–1261, Mar. 2014.

[29] J. Sun, "Small-signal methods for AC distributed power systems—A review," *IEEE Trans. Power Electron.*, vol. 24, no. 11, pp. 2545–2554, Nov. 2009.

[30] J. Sun, "Impedance-based stability criterion for grid-connected inverters," *IEEE Trans. Power Electron.*, vol. 26, no. 11, pp. 3075–3078, Nov. 2011.

[31] J. Wu, J. Wen, H. Sun, and S. Cheng, "Feasibility study of segmenting large power system interconnections with AC link using energy storage technology," *IEEE Trans. Power Syst.*, vol. 27, no. 3, pp. 1245–1252, Aug. 2012.

[32] *2.7V 650-3000F Ultracapacitor Cells*. Accessed: Dec. 20, 2020. [Online]. Available: https://www.maxwell.com/images/documents/K2Series_DS_1015370_5_20141104.pdf

[33] X. Lu, K. Sun, J. M. Guerrero, J. C. Vasquez, and L. Huang, "State-of-charge balance using adaptive droop control for distributed energy storage systems in DC microgrid applications," *IEEE Trans. Ind. Electron.*, vol. 61, no. 6, pp. 2804–2815, Jun. 2014.

[34] M. Liserre, T. Sauter, and J. Hung, "Future energy systems: Integrating renewable energy sources into the smart power grid through industrial electronics," *IEEE Ind. Electron. Mag.*, vol. 4, no. 1, pp. 18–37, Mar. 2010.

[35] A. M. Roslan, K. H. Ahmed, S. J. Finney, and B. W. Williams, "Improved instantaneous average current-sharing control scheme for parallel-connected inverter considering line impedance impact in micro-grid networks," *IEEE Trans. Power Electron.*, vol. 26, no. 3, pp. 702–716, Mar. 2011.

[36] J. Yang, X. Jin, X. Wu, P. Acuna, R. P. Aguilera, T. Morstyn, and V. G. Agelidis, "Decentralised control method for DC microgrids with improved current sharing accuracy," *IET Gener., Transmiss. Distrib.*, vol. 11, no. 3, pp. 696–706, Feb. 2017.

[37] X. Li *et al.*, "Rolinkt and autonomous DC link voltage control and stability analysis for a DC microgrid," in *Proc. Int. Power Electron. Motion Control Conf.*, Hefei, China, May 2016, pp. 3708–3714.

[38] G. Zhang, X. Tang, L. Zhou, and Z. Qi, "Research on complementary PWM controlled buck/boost bi-directional converter in supercapacitor energy storage," *Proc. CSEE*, vol. 31, no. 6, pp. 15–21, Feb. 2011.
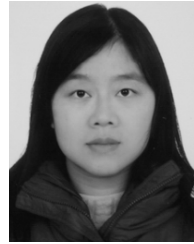
TENG LI (Member, IEEE) was born in Hebei, China, in 1978. She received the B.S. degree in electrical engineering from North China Electric Power University, Baoding, China, in 2000, and the M.Sc. and Ph.D. degrees in analytical science and instrumentation system from The University of Manchester, U.K., in 2004 and 2009, respectively.

From May 2008 to April 2010, she worked at the U.K. Research Centre in NDE (RCNDE), as a Postdoctoral Fellow. She has been an Associate Professor with the School of Electrical Engineering, Beijing Jiaotong University, since 2014. Her current research interests include power supplies for electric railways, on-line monitoring and diagnosis of the power system and its key devices, and the analysis of the power system stability.

YONGJUN ZHOU was born in Hebei, China, in 1994. He received the B.S. degree in electrical engineering from the North China University of Science and Technology, Tangshan, China, in 2018. He is currently pursuing the master's degree with the School of Electrical Engineering, Beijing Jiaotong University.

His current research interests include theory of traction power systems and its power quality analysis.

MINGLI WU (Member, IEEE) was born in Hebei, China, in 1971. He received the B.S. and M.S. degrees in electrical engineering from Southwest Jiaotong University, Chengdu, China, in 1993 and 1996, respectively, and the Ph.D. degree in electrical engineering from Beijing Jiaotong University, Beijing, China, in 2006.

He has been a Professor with the School of Electrical Engineering, Beijing Jiaotong University, since 2008. His current research interests include power supplies for electric railways, digital simulation of power systems, and electric power quality.

TINGTING HE received the B.E. and master's degrees in electrical engineering from Beijing Jiaotong University, Beijing, China, in 2012 and 2014, respectively, and the Ph.D. degree in electrical engineering from the University of Technology Sydney (UTS), Sydney, Australia, in 2018. She was a Casual Academic with the Faculty of Engineering and IT, UTS, from 2015 to 2018. She is currently a Postdoctoral Fellow with Beijing Jiaotong University. Her research interests include power electronics, electric vehicles, and predictive control.

● ● ●